Catalysis Communications 179 (2023) 106694

Contents lists available at ScienceDirect

Catalysis Communications

journal homepage: www.elsevier.com/locate/catcom

Delaminated hydrotalcite precursors for green methanol synthesis

James Hayward [a], Jonathan Ruiz Esquius [a], Nia Richards [a], Wilm Jones [b,c], Daniel Hewes [a], Michael Bowker [a,b,*]

[a] Cardiff Catalysis Institute, School of Chemistry, Cardiff University, Cardiff CF10 3AD, UK
[b] UK Catalysis Hub, Research Complex at Harwell, Rutherford Appleton Laboratory, Harwell, Oxon OX11 0FA, UK
[c] Finden Ltd., Rutherford Appleton Laboratory, Building R71, Office 1.12-13 Harwell Campus, Didcot OX11 0QX, UK

ARTICLE INFO

Keywords:
Green methanol
CO2 hydrogenation
Methanol synthesis
Hydrotalcite
Delamination
Copper catalyst

ABSTRACT

Co-precipitation was used to prepare a copper, zinc, and aluminium hydrotalcite-like precursor to make a methanol synthesis catalyst. Treatment of the wet precursor with an aqueous miscible organic solvent led to the delamination of the sheet-like structure of the precursor phase, dramatically increasing the surface area to 340 $m^2\ g^{-1}$ in comparison to 22 $m^2\ g^{-1}$ for the untreated material. We show that the copper is initially sequestered within the hydrotalcite phase, and during calcination a CuO phase evolves out from the lamellar structures. Reduction proceeds to Cu^0, and neither the calcination nor reduction of the material cause the loss of the lamellar morphology. This leads to high Cu^0 surface areas in the final catalyst (66 $m^2\ g^{-1}$) and high activity in the methanol synthesis reaction.

1. Introduction

With the continuing rise in global CO_2 levels, and its links to anthropogenic climate change, there has been an increasing drive towards greener technologies involving the capture, sequestration and utilisation of CO_2 [1]. The hydrogenation of CO_2 to produce methanol is an attractive method of utilisation as methanol has a broad range of possible applications, such as in fuels or as a chemical precursor. It is also possible that this synthesis can be carried out in a fully green manner; by using recaptured CO_2 and hydrogen generated from renewable sources such as solar powered electrolysis of water, for example [2]. This can allow the process to also be used as a hydrogen storage method, further enhancing its green credentials. The concept of using CO_2 and methanol in these manners was popularised by Olah, who referred to it as the anthropogenic carbon cycle [3].

Methanol production currently stands at 110 Mtons *per annum* from over 90 plants around the world [4]. The primary method of production is from a mixture of carbon monoxide, carbon dioxide, and hydrogen (syngas) at elevated pressures and moderate temperatures. The process for methanol from CO_2 hydrogenation differs in that the feed gas does not contain carbon monoxide, and follows the following reaction scheme (1):

$$CO_2 + 3\ H_2 \rightarrow CH_3OH + H_2O \quad (1)$$

In the industrial synthesis, the carbon monoxide present in the feed undergoes the water-gas shift reaction (2) with the water produced, giving the overall reaction stoichiometry of (3).

$$CO + H_2O \rightarrow CO_2 + H_2 \quad (2)$$

$$CO + 2\ H_2 \rightarrow CH_3OH \quad (3)$$

Due to the lack of carbon monoxide in the feed gas, the products from CO_2 hydrogenation will contain much higher proportions of water

The catalysts used to perform either form of the reaction are predominantly $Cu/ZnO/Al_2O_3$ materials, typically synthesised by coprecipitation of a zincian malachite precursor. A large body of research exists regarding this system, and it is widely accepted that high copper surface areas and the presence of zinc oxide in close proximity to the copper are required for a high activity catalyst [5].

Another potential precursor that has been investigated is copper-modified hydrotalcites. Hydrotalcites belong to a category of material known as a layered double hydroxide (LDH), which are represented by the formula $[M^{2+}_{1-x}M^{3+}_x(OH)_2](A^{n-})_{x/n}{\cdot}mH_2O$ [6]. The archetypal hydrotalcite consists of Mg^{2+} and Al^{3+} in brucite-like layers of octahedrally coordinated metal hydroxides with carbonate CO_3^{2-} as an intercalated anion (see Fig. 1), but a wide range of viable substitutions for the M^{2+} (Ca^{2+}, Zn^{2+}, Ni^{2+}, Cu^{2+}, Co^{2+}, Fe^{2+}) and M^{3+} (Cr^{3+}, Ga^{3+}, Y^{3+}, Mn^{3+}) cations exist [7–11].

* Corresponding author at: Cardiff Catalysis Institute, School of Chemistry, Cardiff University, Cardiff CF10 3AD, UK.
E-mail address: bowkerm@cardiff.ac.uk (M. Bowker).

https://doi.org/10.1016/j.catcom.2023.106694
Received 3 March 2023; Received in revised form 28 April 2023; Accepted 7 May 2023
Available online 8 May 2023

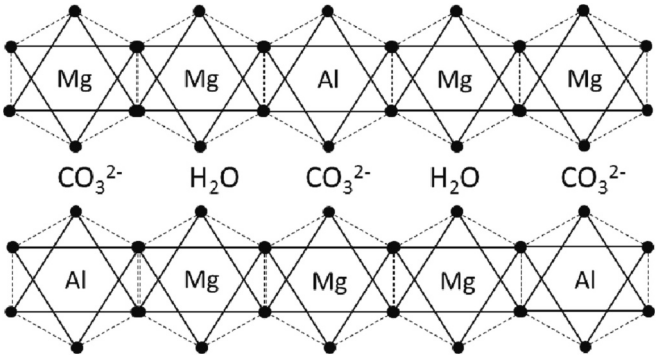

Fig. 1. Schematic representation of the structure of hydrotalcite.

The substitution of copper into these materials faces an additional complication, in that Jahn-Teller distortions of the octahedral structure can lead to destabilisation of the hydrotalcite lattice. Nonetheless, numerous examples of partially substituted Cu-containing materials exist in the literature; of particular interest is the substitution of both copper and zinc as the M^{2+} cation, as this generates a material with the same elements as the $Cu/ZnO/Al_2O_3$ methanol synthesis catalysts [12]. These materials have usually suffered from low overall surface areas as the layers of the lamellar structure aggregate upon drying [13].

Numerous methods have been employed to delaminate the hydrotalcite phase to produce higher surface area materials, but these generally require the use of expensive surfactants and exfoliation techniques [14–17]. However, a method was developed by O'Hare et al. in which the material was prevented from aggregating upon drying, thereby generating a high surface area without the need of exotic techniques. This was achieved simply and cost effectively through the replacement of the inter-layer water with an aqueous-miscible organic solvent, which is then removed in the drying step [18–20].

The initial research into this method was used to allow for the redispersion of hydrotalcites in organic media, and in this study we assess the ability of the technique to generate high surface area catalyst precursors for methanol synthesis catalysts. The catalysts generated from the hydrotalcites are compared to catalysts generated from the conventional zincian malachite precursor, and also against a commercial methanol synthesis catalyst.

2. Results and discussion

The preparation of the materials used in this work are described in the experimental section below. The objectives were to prepare Cu and Zn substitutes hydrotalcite materials, and to make them with very high surface area, much higher than normal $Cu\text{-}ZnO\text{-}Al_2O_3$ (CZA) type materials. The latter are generally made by co-precipitation of nitrates with sodium carbonate, to produce a hydroxycarbonate material with malachite-type structure. Here we approach the problem using Cu and Zn substituted hydrotalcites and use delamination of those precursors to make higher area materials in which Cu is supported on the oxidic layers. Untreated copper zinc aluminium hydrotalcite is labelled CZA—U, and the delaminated material (which undergoes a delamination treatment prior to drying) is labelled CZA-DL, while zincian malachite is ZM. The calcined CZA-DL is labelled CZA-DL-C, the reduced version is CZA-DL-R and the post-reaction material is CZA-DL-PR.

2.1. Composition and structure

The precursors, after preparation and drying at 110 °C for 16 h, were analysed by XRD, MP-AES and EXAFS. The XRD patterns of the precursor materials are shown below in Fig. 2. The ZM precursors displayed an XRD peak pattern characteristic of the malachite phase (ICDD 01–075-1163), indicating the successful formation of the intended

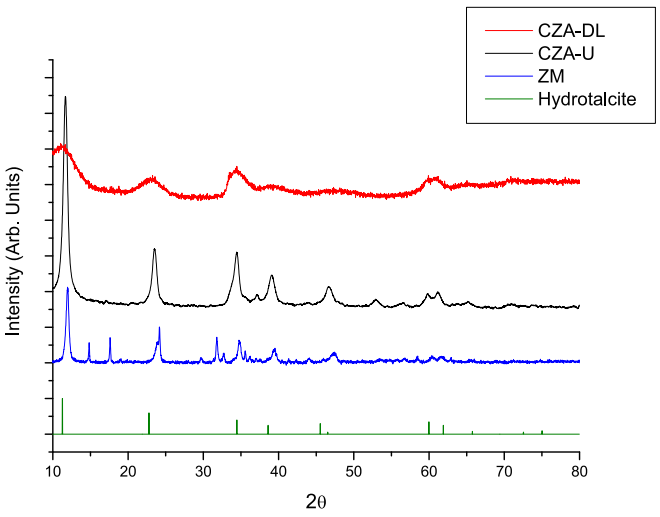

Fig. 2. Powder XRD patterns of the copper zinc aluminium hydrotalcite (CZA—U, middle), treated CZA-DL (top) and ZM (bottom) precursors. Reference pattern of Mg hydrotalcite (ICDD 00–022-0700) included.

hydroxycarbonate. The peaks are sharp, indicative of a low area material. The CZA-U precursors displayed a slightly shifted pattern when compared to a pure hydrotalcite phase, which is thought to be due to the substitution of the magnesium in such a system with zinc and copper in our material. Nonetheless the peak positions and relative intensities are otherwise consistent with a zinc-based hydrotalcite (ICDD 01–074-2703). The treated CZA-DL precursors display broadened peaks at similar angles to the untreated CZA-U precursor pattern, which would indicate that a similar material has been formed. The broadening is probably due to the beginning of delamination, and is particularly evident in the [003] peak at 11.7°. However, the presence of peaks indicates that the material has not been fully delaminated, as a single layer of material would not produce such an XRD pattern. When these materials are heated then the delamination becomes much clearer. Fig. 3, shows a complete loss of the [003] peak, and also of the [006] peak at 23°. This is thought to be indicative of the delamination treatment resulting in replacement of the interlayer water with acetone, which is then driven out by heating to affect the delamination. The other peaks are very broad, except there appear to be the formation of very small amounts of other phases, mostly malachite, of low area (sharp peaks).

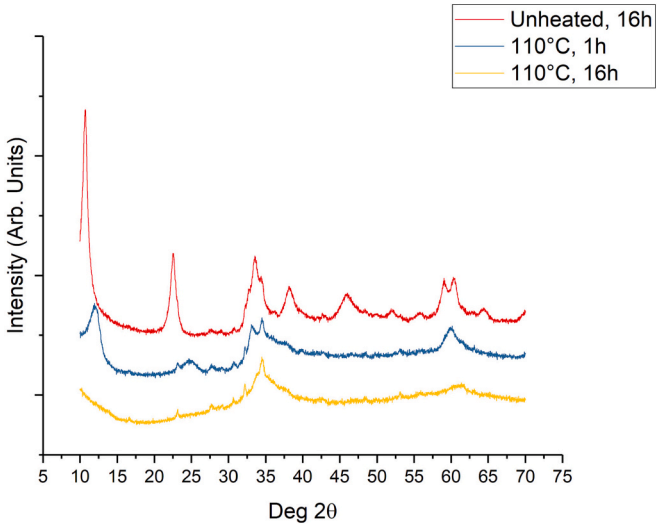

Fig. 3. XRD of the precursor material (CZA-DL) before and after drying at 110 °C for different times.

The different morphologies of the precursors can be seen through electron microscopy. SEM images show the aggregated plate-like structures of the hydrotalcites compared to the more rod-like structures of the malachite precursors (Fig. 4). The delaminated morphology of the treated CZA-DL precursors can be clearly seen by TEM (Fig. 5), with the thin sheets easily distinguished from the more aggregated arrangement of the untreated precursors. There do not appear to be any discrete particles visible for either of these precursors, indicating that the component elements are distributed throughout these sheets.

Analysis of the precursors by microwave plasma atomic emission spectroscopy confirmed that all precursor materials had a composition of 50% Cu, 25% Zn and 25% Al with an error of approximately ±1%.

We carried out XAS measurements on our samples. Cu K-edge interpretation is challenging due to the multiplicity of final states (3d, 4p or 4 s), containing multiple absorption features. Cu- K-edge E_0 values were obtained from the first derivative corresponding to the 1 s-4p electronic transition. Energies associated with 1 s-3d, 1 s–4 s and 1 s-4p Cu K-edge electronic transitions obtained from the first derivative can be found in Table 1 (the derivative curves for the XAS are shown in the supplementary information, Figs. S1 and S2). Transition energies obtained for Cu, Cu_2O and CuO standards agree with energy values reported previously for similar materials [21,22].

The normalised XANES of the dried and calcined CZA-DL samples (Fig. 6) shows that the 1 s-4p transition at 8996.0 eV falls between values observed for Cu_2O (8995.5 eV) and CuO (8997.3). Pre-edge absorption (1 s-3d transition) was observed (see Fig. 6 insert), which suggested a Cu^{2+} oxidation state, and the general form of the spectra seems to more closely resemble Cu^{2+} than Cu^{+}. The lower pre-edge absorption energy of the dried material compared to CuO might indicate a change in the metal ion symmetry from octahedral to tetrahedral as observed for $CuAl_2O_4$; for a tetrahedral configuration, the 1 s-3d transition is more favourable and translates in a higher intensity pre-edge absorption [23]. A decrease in the ligand field strength and a less distorted CuO_6 octahedron compared to CuO can also account for the shift towards lower absorption energy [23]. It has been reported that Cu-containing hydrotalcites where the Cu is in an octahedral coordination environment [22] show smaller pre-edge peak area and peak height compared to tetrahedral and square planar Cu complexes [24]. In our case, a relatively small pre-edge peak area of 0.018 and peak height of 0.009 observed for the dried sample suggests a Cu octahedral environment. The XANES previously reported for Cu-containing hydrotalcite with a small pre-edge and without an evident 1 s - 4 s transition [22] suggests that the Cu in our dried sample is contained within the hydrotalcite structure.

After calcining in air (350 °C, 3 h), XANES for the calcined material remains like that of CuO (Fig. 6). The 1 s-3d pre-edge adsorption is shifted towards higher energy compared to the dried material, which suggests a stronger Jahn-Teller effect, associated with a higher octahedral distortion, yet indicates a Cu^{2+} oxidation state. A shoulder associated with the 1 s–4 s transition close to that of CuO was observed, and the 1 s-4p energy transition shifted towards higher energy, closer to the CuO standard, with a decrease in the absorption intensity. Linear combination fitting (Table S1) using the dried material as a standard for hydrotalcite suggests that 62% of the Cu evolved from the lattice as CuO after annealing, 33% stayed within the hydrotalcite and the remaining 5% was assigned to Cu_2O (Table S1). No metallic Cu was detected. After reduction (225 °C, 1 h), no CuO-like pre-edge absorption was observed for the treated CZA-htl materials indicating that Cu in the sample had an oxidation state lower than Cu^{2+}. Absorption energies for 1 s–4 s and 1 s-4p transitions were close in energy to the Cu_2O standard, however a shoulder at 9001 eV associated with Cu^0 was observed (Fig. 7). Features above this energy were lacking, which suggested little long-range order. This might be associated with small Cu nanoparticles. XAS was measured *ex-situ* and materials had been exposed to air prior to and during analysis, thus, we hypothesise that a realistic picture of the post-reduction material is as small Cu particles, which became passivated in contact with air [25,26]. Note however that Kühl et al. [12], Günter et al. [27] and Kleymenov et al. [21] showed that CuO first reduces to Cu_2O before being fully reduced to Cu, and that after reduction at mild temperature a mixture of metastable Cu_2O and Cu co-exists [25].

The intensity of the 1 s-4p transition after reaction intensified, whilst the peaks associated to 1 s-3d and 1 s-3d transitions dampened and shifted towards lower binding energy compared to the reduced material. Moreover, characteristic features of Cu-foil up to 9300 eV, including the peak at 9035 eV, were observed indicating that more complete reduction and possibly some sintering had occurred during reaction (Fig. 7).

XAS of the Zn K-edge for the treated CZA-DL samples was also carried out and compared against XANES for ZnO and Zn foil used as standards (Fig. 8). The first absorption edge for the dried material was not well defined, but was broader, more intense and shifted towards higher binding energy (from the first derivative as shown in Fig. S2) compared to ZnO, which suggests an octahedral coordination in accordance with that observed on the Cu K-edge [28]. Moreover, the XANES spectra for CZA-DL dried resembles that reported for a Zn/Al-hydrotalcite [29], further confirming that Cu and Zn for CZA-DL dried sample are within a hydrotalcite structure as suggested by XRD. The first absorption edge for the calcined material was more defined than for the dried one, but with lower white line intensity, whilst the first scattering resonance around 9668 eV is damped. This might suggest that some Zn^{2+} oxide centres changed from octahedral to tetrahedral coordination [28,30]. No long-range featured were observed indicating small particle size or an amorphous matrix. The Zn adsorption edge for the reduced material was at the same energy as ZnO, indicating that Zn^{2+} was not reduced. However, the adsorption edge decreased in intensity and the first resonance peak shifted towards higher binding energy, which could be associated to ZnO-Cu interactions [26]. No significant differences in

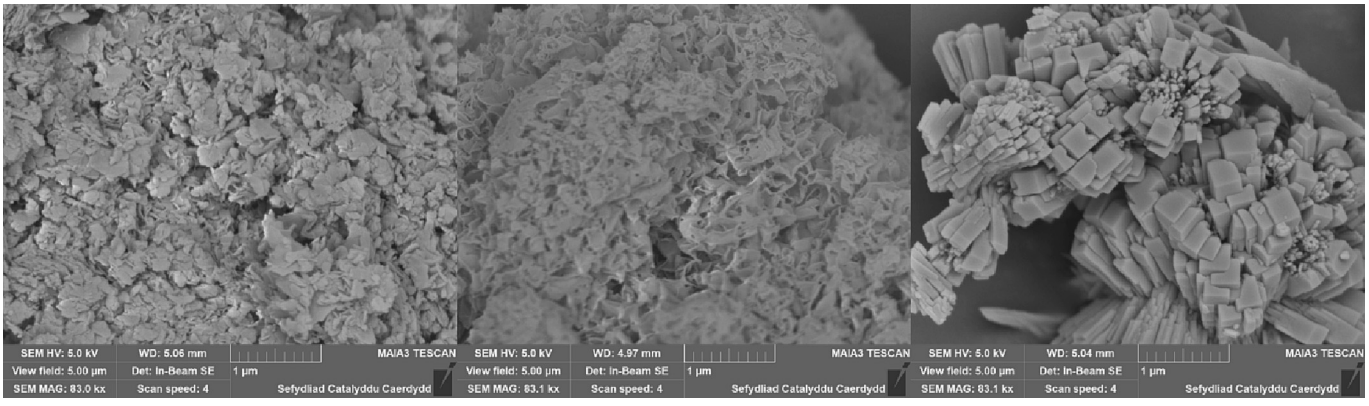

Fig. 4. SEM images of the catalyst precursor materials. Left: CZA-U Middle: Treated CZA-DL Right: Zincian malachite.

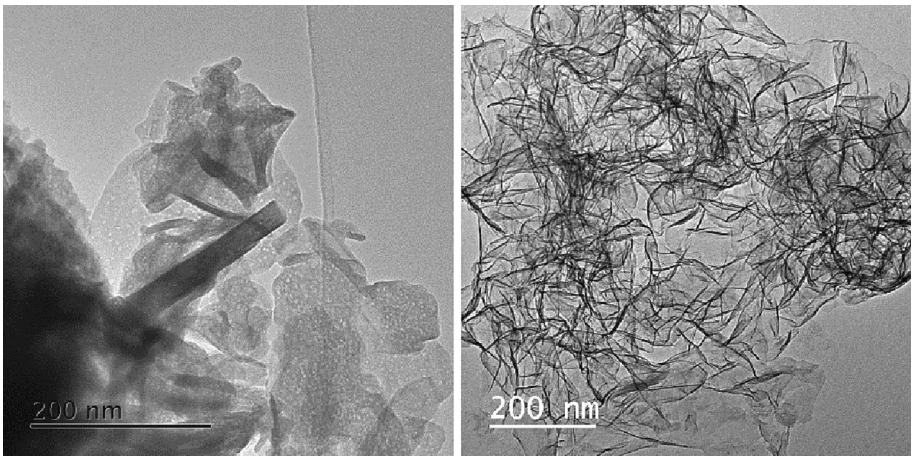

Fig. 5. TEM images of the catalyst precursor materials. Left: CZA—U, image size 500 × 500 nm.; Right: the CZA-DL, image size 800 × 800 nm.

Table 1
Cu K-edge electronic transitions obtained from the first derivative for treated CZA-DL following different treatments.

Sample	1 s-3d / eV	1 s–4 s / eV	1 s-4p / eV / E_0
Cu		8981.1	8993.4
Cu_2O		8981.5	8995.5
CuO	8978.2	8985.8	8997.3
CZA-DL (dried)	8977.5	8988.0	8996.0
CZA-DL-C (calcined)	8977.8	8987.1	8996.6
CZA-DL-R (reduced)		8981.5	8995.9
CZA-DL-PR (post-reaction)		8981.3	8994.3

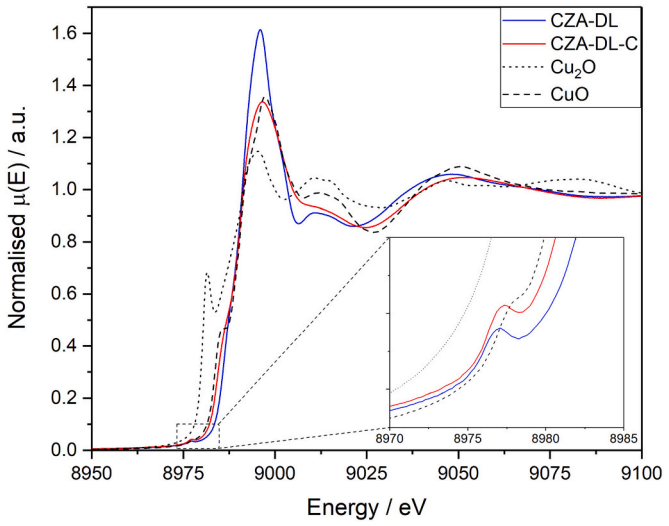

Fig. 6. Normalised Cu K-edge XANES for CZA-DL samples; dried and calcined samples are compared to Cu_2O and CuO standards.

XANES were observed between the reduced and post-reaction samples.

2.2. Surface areas and particle sizes

The surface areas of the treated CZA-DL are significantly higher than untreated samples and are significantly higher than the malachite-based materials. This is due to the effect of the delamination of the samples, with the large amounts of individual wafers presenting a far higher amount of exposed surface, as can be seen in the TEM (Fig. 5). Whilst some of this surface area is lost after calcination, the surface areas seem relatively constant across the range of calcination temperatures

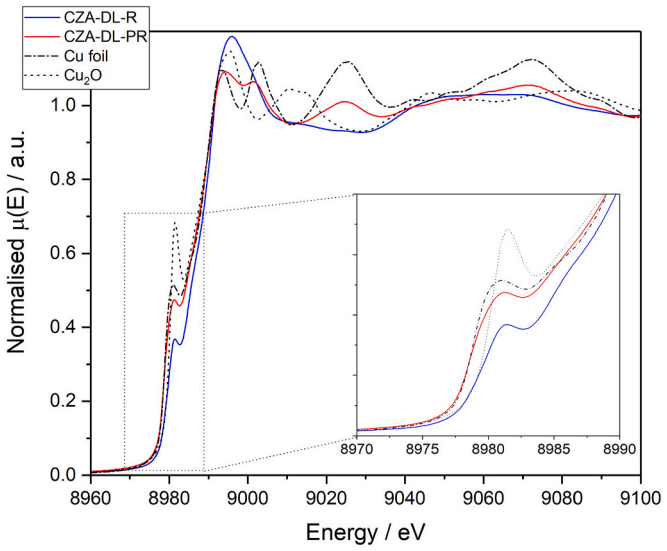

Fig. 7. Normalised Cu K-edge XANES for CZA-DL samples; reduced and post-reaction samples are compared to Cu and Cu_2O standards.

(Table S2).

An *in situ* calcination study on the delaminated hydrotalcite precursors shows that the initial hydrotalcite peaks have disappeared entirely by 200 °C, and there is then no observable change until 500 °C when peaks at 35.5° and 38.8° increase in intensity (Fig. 9). These are consistent with copper (II) oxide (ICDD 01–089-5898). Whilst the overall surface area of the material has reduced, it is still high (179 m^2 g^{-1}), and the XRD implies that the copper oxide is segregating out of the lattice and forming particles. This is borne out by the TEM images of these materials, which show evidence of both the wafer structure and larger crystallites of copper oxide (Fig. 10). This is thought to be due to the calcination temperature of this sample exceeding the Tamman temperature of copper oxide (527 °C), leading to significant Cu mobility in the material. The zinc and aluminium phases possess higher melting points and thus higher Tamman temperatures (851 and 899 °C respectively), meaning that the overall lamellar structure is retained.

Below the 500 °C calcination temperature there are no significant changes in diffraction peaks observed in the XRD patterns (Fig. 9), nor any definable nanoparticles in TEM imaging (Fig. 10). However, after *in situ* reduction at 200 °C for 1 h broad peaks at 43.1° and 50° can be assigned to the Cu (111) and (200) planes respectively, indicating the formation of copper nanoparticles (ICDD 01–070-3038) (Fig. 11).

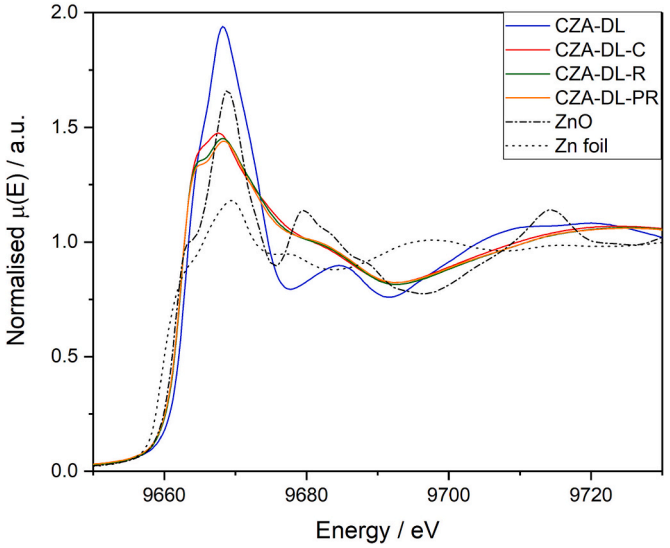

Fig. 8. Normalised Zn K-edge XANES for CZA-DL samples; dried, calcined, reduced and post-reaction samples are compared to Zn and ZnO standards.

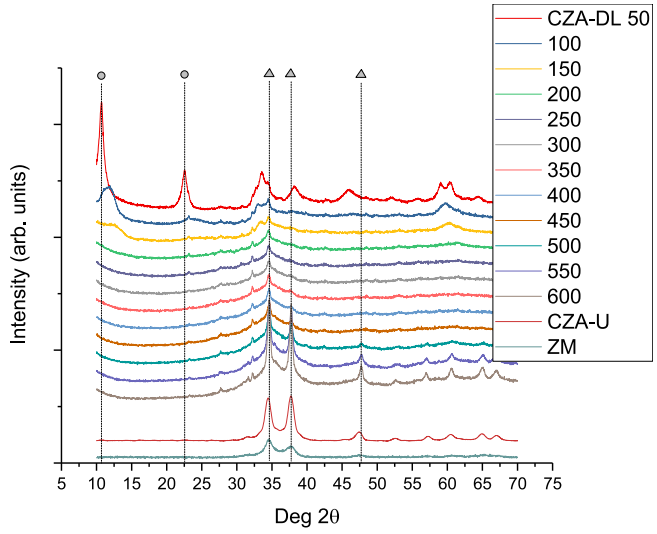

Fig. 9. Powder XRD peak patterns of CZA-DL materials after calcination at different temperatures. ● – hydrotalcite main peak positions, ▲ CuO main peak positions.

Application of the Scherrer equation to the Cu (111) plane gives an average nanoparticle size of 4 nm for the delaminated sample. TEM images of a reduced sample of CZA-DL-R (Fig. 12) show the presence of nanoparticles distributed across the sheets, which are assumed to be the copper seen by XRD analysis.

By comparison, the untreated CZA-U materials show sharp peaks in the XRD traces, with the phases being assigned to copper oxide (01–089-5898). By the Scherrer equation these have particle sizes of 8–9 nm (Fig. 9), and after *in situ* reduction at 200 °C for 1 h peaks equivalent to the Cu (111) and (200) planes are seen (Fig. 11). Interestingly, by the Scherrer equation the CZA-U materials have a slightly lower average Cu nanoparticle size of 6–7 nm after reduction, although this is not reflected in their copper surface areas. This is thought to be due to most of the copper being unavailable at the surface, and they are trapped within the bulk of the material.

The ZM catalyst displays the expected copper oxide pattern (ICDD 01–089-5898) upon calcination and copper metal nanoparticles post reduction (Fig. 11). In both cases the particle size by the Scherrer equation is 10 nm.

The copper specific surface areas of the materials (as determined by N_2O titration) follow the trend of the overall surface area, with the CZA-DL materials having the highest (66 $m^2\ g^{-1}$) and the CZA-U materials having the lowest (~1 $m^2 g^{-1}$), Table 2. It was expected that the treated CZA-DL material would have the highest copper specific surface area due to the combination of high overall surface area and small copper particles. Conversely, whilst the relatively small copper metal particles of the untreated CZA-U would imply a higher copper surface area, it is thought that the majority of this copper is occluded within the bulk of the low surface area material, leading to a lower amount of exposed surface compared to the ZM and treated CZA-DL materials.

The delamination treatment appears to have a significant effect on the reducibility of the copper as determined by TPR (Fig. 13). The CZA-U displays peaks with an initial onset of 180 °C and peaks at 205, 235, 266, 295, and 318 °C. By contrast CZA-DL shows a lower onset temperature and a much narrower peak profile. For CZA-DL the reduction is complete at 295 °C compared to 340 °C with CZA—U. This increased reducibility of the CZA-DL sample is likely to play a role in its improved catalytic performance.

2.3. Catalytic testing

The activity and selectivity of the different materials in the CO_2 hydrogenation reaction was studied at 20 bar using a gas mixture of 20% CO_2, 60% H_2, and 20% N_2. The catalysts were analysed across a temperature range of 200–250 °C with a dwell time of 16 h at each temperature. Initially the catalysts were pressed at 5 t pressure and sieved, with the 425-600 μm fraction being retained for testing. The results of this testing are shown below in Table 3.

Samples of the treated CZA-DL that were pressed at lower pressure (0.2 t) showed a little better conversion and methanol productivity. Unpressed samples (*i.e.* tested in powder form) showed lower CO_2 conversion, because only 1/5th of the material was used, but had greatly increased methanol productivity; the low density of the material necessitated a lower catalyst mass to be loaded into the catalyst tube volume. Although the delaminated catalysts had higher total surface area and copper surface area, with this amount of catalyst in the same reactor volume, they showed only mild improvements over the untreated hydrotalcites, and were comparable to the zincian malachite and industrial catalysts at temperatures above 200 °C. This is because the low density treated hydrotalcites were extremely compressible during the pressing process, and further investigation showed that the surface area of the treated CZA-DL catalyst falls from ~250 to 74 $m^2\ g^{-1}$ upon pressing. The material was also observed to have lost its easily distinguished lamellar structure when ground and analysed by TEM. We believe that the higher pressing pressures used have, in effect, relaminated the material. All the samples showed no discernible decline in activity with time. For instance sample CZA-DL B showed an average conversion of 18.6%, averaged over 4 measurements each four hours apart, with a random mean variation of ±0.4%.

Although the increased productivity is desirable, the loss of surface area upon compression presents an obvious issue for potential industrial applications, where the catalyst would need to be treated in such a way that it can withstand the conditions of pelleting and use in a full-scale gas phase reactor. Investigations would need to be conducted into alternative methods of improving the structural characteristics of the material during processing to maintain the lamellar structure, and the addition of binder agents of the right type, as is usually done industrially prior to pelleting, would probably be beneficial for the maintenance of lamellae separation. Such binders are of various types including oils which can convert to carbon-type species, cements, and other irreducible oxides. It is possible compression could be avoided by making spherical beads including the lamellar material in a silica matrix. These would then be calcined, but as shown above, the lamellar structure survives calcination. Further it may be possible to use lower

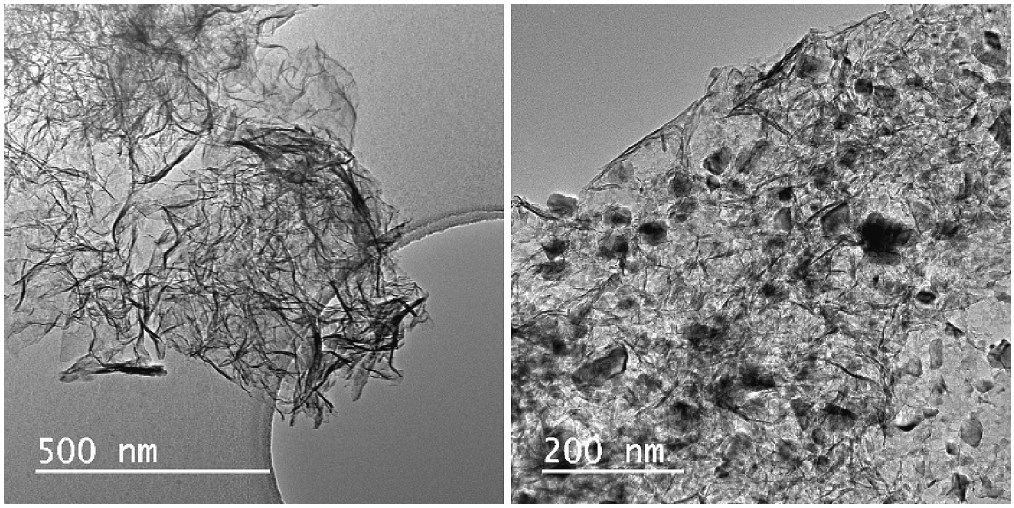

Fig. 10. TEM images of treated CZA-DL-C materials calcined at 350 °C (left image) and 600 °C (right image).

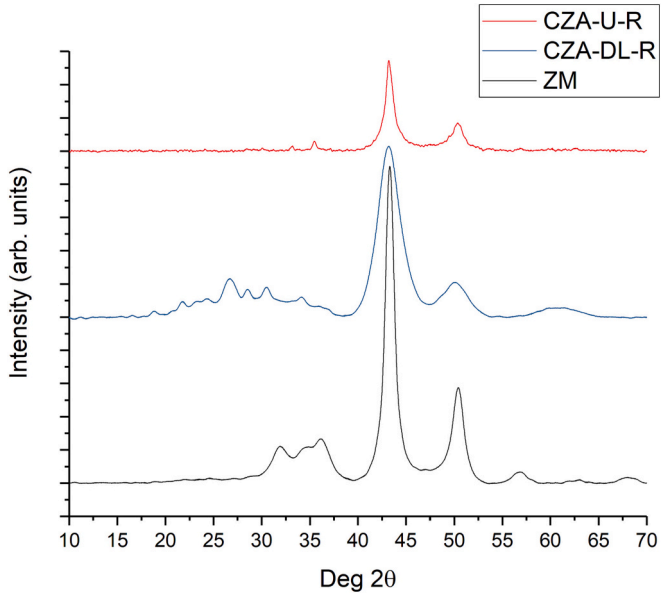

Fig. 11. Powder XRD patterns of ZM, CZA-U and treated CZA-DL-R after reduction. Top: CZA-U-R; Middle: CZA-DL-R; Bottom: ZM-R. Conditions: 5% H_2/Ar, 30 ml min^{-1}, 200 °C, 1 h.

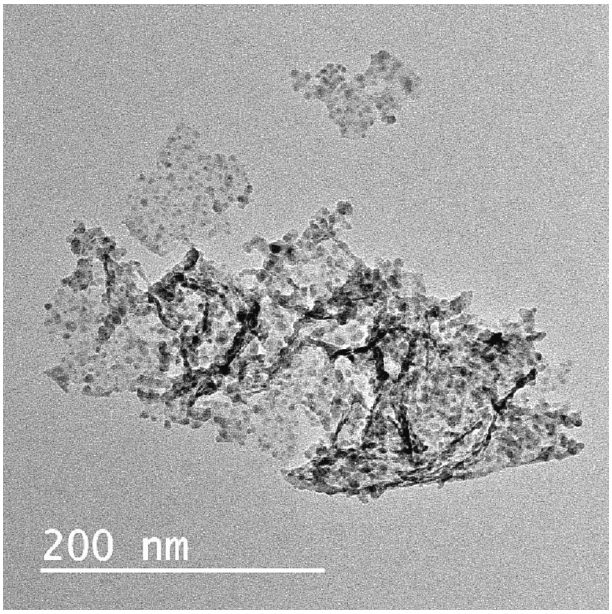

Fig. 12. TEM of CZA-DL-R after reduction at 400 °C for 1 h in 5% H_2/Ar.

compression pelletisers.

The situation could be different in the liquid phase where pelleting would not be needed. There is currently much experiment and discussion regarding the possibilities of liquid phase, solvent-based methanol synthesis, since this may afford the possibility of operating both at very high pressure and low temperature, thus favouring higher equilibrium yields [31,32].

3. Methods

3.1. Synthesis

All materials in this study were prepared by coprecipitation of copper nitrate hemipentahydrate, zinc nitrate hexahydrate, and aluminium nitrate nonahydrate using a Metrohm Titrando Autotitrator. For the malachite-based precursors (ZM) sodium carbonate was used as the precipitating agent, with the synthesis taking place at a pH of 6.5 and a temperature of 65 °C with a 3 h aging time.

Table 2
Total surface areas for precursor and calcined materials, with Cu^0 surface areas and Cu^0 particle sizes for the reduced materials. Precursor: dried 110 °C 16 h; calcined: 350 °C 3 h; Cu^0: reduced at 225 °C for 1 h in 5% H_2/Ar.

	Surface areas			XRD Particle sizes
	Precursor (m^2g^{-1})	Calcined (m^2g^{-1})	Cu^0 (m^2g^{-1})	(nm)
ZM	77	80	31	10
CZA-U	22	16	1	7
CZA-DL	340	250	66	4

The hydrotalcite materials (CZA—U) were precipitated using a mixture of sodium hydroxide and sodium carbonate at a pH of 9 and a temperature of 25 °C. No aging was used. The standard hydrotalcites were filtered, washed with deionised water, and dried at this point, whereas the treated hydrotalcites (CZA—DL) were filtered, washed with

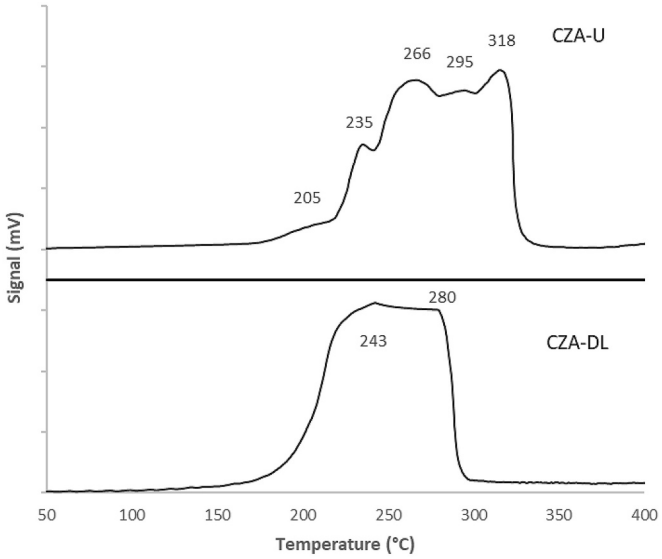

Fig. 13. TPR of 100 mg CZA-U and CZA-DL between 50 and 400 °C 10% H_2/Ar. Thermal ramp rate 5 °C min^{-1}.

ethanol, and redispersed in acetone for 1 h. This redispersed material was then filtered, washed with acetone, and dried.

All materials were initially prepared with a 2:1:1 M ratio of Cu:Zn:Al for comparative purposes. All materials were initially calcined at 350 °C for 3 h under flowing air to give the catalyst material.

3.2. Catalyst characterisation

Powder X-ray diffraction measurements were performed using a PANalytical X'pert Pro diffractometer with Ni filtered CuKα radiation source operating at 40 kV and 40 mA. Patterns were recorded over the range of 10–80° 2θ using a step size of 0.016°. All patterns were matched using the ICDD database.

Transmission electron microscopy (TEM)-EDX used the JEOL-2100 EM system with a LaB_6 filament operating at 200 kV. Catalyst samples were prepared by dispersing the sample in ethanol before transfer to a lacey carbon-coated Cu grid.

In situ XRD studies were conducted using an Anton Parr XRK900 cell (internal volume of ~0.5 L) was used to monitor the formation, size, and stability of metallic Cu particles in the Cu/ZnO/Al_2O_3 materials under reduction and reaction-like conditions. A flow of 5% H_2/Ar (30 ml min^{-1}) was passed through the sample bed while the cell was heated to 225 °C (ramp rate 5 °C min^{-1}). The cell was maintained under these conditions for 1 h, with repeat 20–80° scans being taken. The gas mixture was then switched to 20% CO_2 / 60% H_2 / 20% N_2 for 3 h with the temperature being maintained at 225 °C. Multiple 20–80° scans were performed during this time. Following this, to simulate the presence of reaction products, water vapour was introduced into the gas stream by means of a bubbler system. This system was heated to 85 °C to introduce 15% moisture content to the gas stream, with the *in situ* cell also being heated to 85 °C to prevent condensation. The cell was maintained at these conditions for 3 h, with multiple 20–80° scans being performed.

Surface area measurements were carried out using the BET isotherm method. A Quantachrome Quadrasorb-evo using N_2 at −196 °C was employed in this capacity, with the samples being prepared for analysis by degassing at 120 °C for 3 h under vacuum conditions.

Cu surface area analysis was carried out on a Quantachrome ChemBET chemisorption analyser equipped with a thermal-conductivity detector (TCD). Calcined samples (50 mg) were reduced to using 10% H_2/Ar (30 ml min^{-1}) with heating to 140 °C at 10 °C min^{-1}, and then to 225 °C at 1 °C min^{-1}. For Cu surface area analysis, catalysts were cooled to 65 °C under He for N_2O pulsing. 12 N_2O pulses (113 μl each) were followed with 3 N_2 pulses for calibration. The amount of N_2 emitted was assumed to amount to one half-monolayer coverage of oxygen and that the surface density of Cu is 1.47×10^{19} atoms m^{-2}.

Structural and electronic changes on the CZA-DL sample after drying (CZA-DL-D, 110 °C, 16 h), calcination (CZA-DL-C, 350 °C, 3 h), reduction (CZA-DL-R, 225 °C, 1 h) and CO_2 hydrogenation (CZA-DL-PR, 200–250 °C, 20 bar P, 8 h) were analysed at the Cu and Zn—K edge by X-ray absorption spectroscopy (XAS). XAS measurements were acquired in transmission mode at B18 beamline of the Diamond Light Source at Harwell, UK. Commercially sourced CuO, Cu_2O, ZnO from Sigma Aldrich were analysed as standards. Cu K-edge and Zn K-edge were calibrated against Cu foil and Zn foil references. X-ray absorption near-edge structure (XANES) data analysis was performed using IFEFFIT with Demeter software package (Athena and Artemis) [33].

TPR analysis was carried out on a Quantachrome ChemBET Pulsar chemisorption analyser equipped with a TCD. Calcined samples (100 mg) were pre-treated in He for 1 h at 120 °C to remove any pre-adsorbed material before cooling to room temperature. For analysis the samples were heated under a flow of 10%H_2/Ar (30 ml min^{-1}) whilst ramping the temperature to 400 °C at 5 °C min^{-1}.

3.3. Catalyst testing

The catalytic performance of catalysts for CO2 hydrogenation was determined in a parallel 16 bed high throughput catalytic reactor. The reactor is of a fixed bed continuous flow design. All reactor beds see the same reaction conditions due to the set up of the system, the gas is fed through a capillary distribution system and mixes with the liquid feed in the headspace above the reactor tube. The pressure is controlled in each bed using an equilibar, and the temperature is controlled by thermocouples located in the surrounding heating block of each set of four reactor tubes that sit in each block. The catalyst (0.2 g, all fractions, or 0.5 g pressed catalyst 425–600 μm) was placed in a stainless steel reaction tube of internal diameter of 4.57 mm. The catalysts were placed in all beds, apart from beds 1, 5, 9 and 13, these were filled with only

Table 3
Conversion and selectivity data for the CO_2 hydrogenation reaction.

	CO_2 Conversion (%)			MeOH Selectivity (%)			MeOH productivity mol kg^{-1} h^{-1}		
	200 °C	225 °C	250 °C	200 °C	225 °C	250 °C	200 °C	225 °C	250 °C
Zincian Malachite	9.1	15.6	18.0	73.1	54.1	34.0	3.2	4.0	3.0
$CuZnAl_2O_3$	10.9	15.7	17.6	68.0	51.5	29.3	3.4	3.8	2.4
CZA-U	6.8	14.9	17.9	73.3	54.3	34.2	2.4	3.9	2.9
CZA-DL A	7.2	15.3	17.8	74.9	53.4	34.1	2.6	3.9	2.9
CZA-DL B	7.6	16.6	18.6	73.2	53.7	34.6	2.6	4.2	3.0
CZA-DL C	3.5	7.0	15.7	83.6	60.7	32.8	7.0	10.0	12.0

Conditions: P 20 bar, flow rate 30 ml min^{-1}, gas composition CO_2:H_2:N_2 1:3:1 Pretreatment: 5% H_2/Ar, 30 ml min^{-1}, 225 °C, 1 h. Catalyst mass 0.5 g, pelleting pressure 5 t, sieve fraction 425–600 μm, with the exception of CZA-DL B (pelleting pressure 0.2 t) and C (not pressed or sieved, tested as 0.1 g loose powder).

silicon carbide (F24, 750 μm). The catalyst was supported on a bed of silicon carbide (F24, 750 μm) to ensure it was in the centre of the isothermal heating zone. The catalyst was mixed with F80 silicon carbide, which has a particle size of 190 μm, to aid dispersion and stop any mass transfer limitations. Prior to the reaction, the catalysts were pre-reduced in a flow of 5% H2/N2 (40 ml min − 1 per reactor bed) for 1 h at 225 °C under atmospheric pressure. Once the reduction was complete the gas was switch to nitrogen whilst the reactors cooled to 125 °C, once at temperature the gas composition was switched to the reaction feed (CO_2:H_2:Ar:N_2 22:54:5:19%). A purge feed of nitrogen, equivalent flow to the reaction feed is used to ensure that no product build up is observed in the downstream lines. The pressure was increased to 20 bar using the gas feed pressure over the equilibars. The flow was set to 30 ml min-1 per reactor bed giving a GHSV of 3600 h-1. The reactions were conducted at 200, 225 and 250 °C, the downstream oven was set to 120 °C to stop any product condensing in the reactor lines. The gas products were analysed *via* online gas chromatography using an Agilent 7890B system with a flame ionisation detector (FID) and TCD. Argon was used as an internal standard. Four injections were taken at each temperature per reactor, a vici valve was switched between the beds to allow sampling of the products. It took *ca.* 8 h to sample all beds, therefore took 32 h to complete one reaction temperature. CO2 conversion was calculated by the change in moles of CO2 compared to calibration runs at 125 °C for each bed. In all cases, methanol, methane and CO were the only products observed. The carbon balance was calculated using the sum of carbon products and feed divided by the blank carbon value. After the reaction, the reactor was depressurised and left under flowing nitrogen (50 ml min^{-1}) until cool.

Credit author statement

Michael Bowker was supervisor of the work and he and James Hayward (JH) were main authors. Jonathan Ruiz Esquius, Nia Richards, Wilm Jones, Daniel Hewes and JH were involved in the experimental work - catalyst synthesis, testing and characterisation.

Declaration of Competing Interest

Michael Bowker reports financial support was provided by Engineering and Physical Sciences Research Council. Michael Bowker reports financial support was provided by European Union.

Data availability

Data will be made available on request.

Acknowledgements

We are grateful to a number of organisations for their support for this work. These include the European Union to the EU for funding through H2020 Spire grant mefCO2 (Grant agreement 637016), EPSRC for funding through grants EP/S030468/1, EP/N010531/1 the Catalysis Hub grants, EPSRC grants EP/R026939/1 and EP/R026815/1. We would like to thank the Cardiff University TEM facility for the microscopy. This research has been performed with the use of some facilities at the Research Complex at Harwell. The authors would like to thank the Research Complex for access and support to these facilities and equipment. The authors wish to acknowledge the Diamond Light Source for provision of beamtime as part of the UK catalysis Hub BAG Access to XAS beamline B18. The authors would like to acknowledge Integrated Lab Solutions (ILS) for the design and manufacture of the high throughput reactor and their continued support and technical expertise.

Appendix A. Supplementary data

Supplementary data to this article can be found online at https://doi.org/10.1016/j.catcom.2023.106694.

References

[1] M. Aresta, A. Dibenedetto, Dalton Trans. (2007), https://doi.org/10.1039/b700658f, 2975-2992.
[2] M. Bowker, ChemCatChem 11 (2019) 4238–4246.
[3] G.A. Olah, A. Goeppert, G.K.S. Prakash, Beyond Oil and Gas: The Methanol Economy, Wiley-VCH, Weinheim, 2018.
[4] Alverdo, IHS Chemical Bulletin, 2016, pp. 10–11.
[5] M. Behrens, Angew. Chem.-Int. Edit. 53 (2014) 12022–12024.
[6] D.G. Evans, R.C.T. Slade, in: X. Duan, D.G. Evans (Eds.), Layered Double Hydroxides vol. 119, Springer-Verlag Berlin, Berlin, 2006, pp. 1–87.
[7] Q. Wang, D. O'Hare, Chem. Rev. 112 (2012) 4124–4155.
[8] G.L. Fan, F. Li, D.G. Evans, X. Duan, Chem. Soc. Rev. 43 (2014) 7040–7066.
[9] N. Blanch-Raga, A.E. Palomares, J. Martinez-Triguero, M. Puche, G. Fetter, P. Bosch, Appl. Catal. B-Environ. 160 (2014) 129–134.
[10] P. Gao, L.S. Zhong, L.N. Zhang, H. Wang, N. Zhao, W. Wei, Y.H. Sun, Catal. Sci. Technol. 5 (2015) 4365–4377.
[11] K. Parida, M. Satpathy, L. Mohapatra, J. Mater. Chem. 22 (2012) 7350–7357.
[12] S. Kuhl, A. Tarasov, S. Zander, I. Kasatkin, M. Behrens, Chem.-Eur. J. 20 (2014) 3782–3792.
[13] M. Behrens, I. Kasatkin, S. Kuhl, G. Weinberg, Chem. Mater. 22 (2010) 386–397.
[14] F. Leroux, M. Adachi-Pagano, M. Intissar, S. Chauviere, C. Forano, J.P. Besse, J. Mater. Chem. 11 (2001) 105–112.
[15] Z.P. Liu, R.Z. Ma, Y. Ebina, N. Iyi, K. Takada, T. Sasaki, Langmuir 23 (2007) 861–867.
[16] J. Bin Han, J. Lu, M. Wei, Z.L. Wang, X. Duan, Chem. Commun. (2008) 5188–5190, https://doi.org/10.1039/b807479h.
[17] K. Cermelj, K. Ruengkajorn, J.C. Buffet, D. O'Hare, J. Energy Chem. 35 (2019) 88–94.
[18] C.P. Chen, M.S. Yang, Q. Wang, J.C. Buffet, D. O'Hare, J. Mater. Chem. A 2 (2014) 15102–15110.
[19] M.M.J. Li, C.P. Chen, T. Ayvali, H.R. Suo, J.W. Zheng, I.F. Teixeira, L. Ye, H.B. Zou, D. O'Hare, S.C.E. Tsang, ACS Catal. 8 (2018) 4390–4401.
[20] J.F. Yu, Q. Wang, D. O'Hare, L.Y. Sun, Chem. Soc. Rev. 46 (2017) 5950–5974.
[21] E. Kleymenov, J. Sa, J. Abu-Dahrieh, D. Rooney, J.A. Van Bokhoven, E. Troussard, J. Szlachetko, O.V. Safonova, M. Nachtegaal, Catal. Sci. Technol. 2 (2012) 373–378.
[22] M. Kockerling, G. Geismar, G. Henkel, H.F. Nolting, J. Chem. Soc. Faraday Transact. 93 (1997) 481–484.
[23] K. Shimizu, H. Maeshima, H. Yoshida, A. Satsuma, T. Hattori, Phys. Chem. Chem. Phys. 3 (2001) 862–866.
[24] M. Sano, S. Komorita, H. Yamatera, Inorg. Chem. 31 (1992) 459–463.
[25] S. Poulston, P.M. Parlett, P. Stone, M. Bowker, Surf. Interface Anal. 24 (1996) 811–820.
[26] D. Grandjean, V. Pelipenko, E.D. Batyrev, J.C. van den Heuvel, A.A. Khassin, T. M. Yurieva, B.M. Weckhuysen, J. Phys. Chem. C 115 (2011) 20175–20191.
[27] M.M. Gunter, B. Bems, R. Schlogl, T. Ressler, J. Synchrotron Radiat. 8 (2001) 619–621.
[28] M.M.R. Bhuiyan, S.D. Lin, T.C. Hsiao, Catal. Today 226 (2014) 150–159.
[29] T.P. Trainor, G.E. Brown, G.A. Parks, J. Colloid Interface Sci. 231 (2000) 359–372.
[30] L. Galoisy, L. Cormier, G. Calas, V. Briois, J. Non-Cryst. Solids 293 (2001) 105–111.
[31] H. Nieminen, A. Laari, T. Koiranen, Processes 7 (2019) 405–429.
[32] S. Xie, W. Zhang, X. Lan, H. Lin, ChemSusChem 13 (2020) 614–659.
[33] B. Ravel, M. Newville, J. Synchrotron Radiat. 12 (2005) 537–541.